3D PRINTING AND ADDITIVE MANUFACTURING
Volume 00, Number 00, 2022
© Mary Ann Liebert, Inc.
DOI: 10.1089/3dp.2022.0152

In Situ Reactive Printing of Aluminum Matrix Composite with Ultra-High Volume Fraction Reinforcement

Chenxi Tian and Atieh Moridi

Abstract

Additive manufacturing (AM) can fabricate intricate structures that are infeasible or uneconomical for conventional manufacturing methods. Its unique capabilities have motivated emergence of several printing technologies and extensive research in material adoption in particular ferrous-, Ti-, and Ni-based alloys. Meanwhile, the large freezing range and high reflectivity of aluminum, a lightweight structural material, greatly reduce aluminum's compatibility with AM. The incompatibility roots from aluminum's unstable behavior in the rapid cyclic thermal conditions in AM and its poor interaction with laser. This hinders the development of laser-based aluminum AM and deteriorates the existing lack of lightweight structural materials in the intermediate temperature range. Aluminum matrix composites (AMCs) have great potential to serve as thermally stable lightweight structural materials, combining lightweight nature of aluminum matrix and strength of reinforcement phases. However, fabrication of AMC largely uses conventional methods, achieving only moderate volume fraction of reinforcement while having limited part complexity compared with AM. To address these challenges, *in situ* reactive printing (IRP) is adopted as a novel AM method, harnessing the reaction product of dissimilar elemental powder mix to fabricate AMC with an ultra-high volume fraction of intermetallic reinforcement. In this study, the effect of titanium addition to elemental aluminum feedstock powder is systematically studied on different aspects, including material processability, microstructural features, and mechanical performances. The results show that IRP can overcome the incompatibility between AM and aluminum and produce AMC with exceptional volume fraction of reinforcements and outstanding stiffness enhancement when compared with existing AM aluminum alloys and other AMCs.

Keywords: additive manufacturing, *in situ* reactive printing, aluminum matrix composite, high volume fraction intermetallic, lightweight material

Introduction

Additive manufacturing (AM), with its capability to fabricate complex structures with significantly reduced material waste, has claimed more and more market shares in the field of manufacturing. Fusion-based methods such as powder bed fusion (PBF) and direct energy deposition (DED) are more widely adopted among various metal AM methods. While PBF excels in higher precision, DED is better for larger build volumes as well as easier adaptation to multimaterial prints. Despite their differences and drawbacks, the established material repository available for stable prints and its continued development are undeniably major contributors to increasing adoption of both PBF and DED methods.

Materials commonly used in conventional manufacturing processes are being adopted in AM, such as stainless steels,[1] the Inconel family,[2,3] various titanium alloys, and some aluminum alloys.[4–6] Aluminum alloys, although widely used as a lightweight structural material in conventional manufacturing processes, lack a similar scale of adoption and development in AM compared with other alloys mentioned before. High reflectivity and large solidification range of most aluminum alloys are challenges in processing these alloys using AM.[7]

While aluminum AM is challenging, it has potential to overcome limitations of conventional cast aluminum alloys. The coarsening and dissolving of precipitates result in lack of thermal stability in conventional cast aluminum alloys to perform as structural materials in the range of 200°C–450°C,

---

Sibley School of Mechanical and Aerospace Engineering, Cornell University, Ithaca, New York, USA.

which is currently filled by ferrous-, Ti-, and Ni-based alloys.[8] AM has shown some potential in creating alloys with a moderate volume fraction of thermally stable precipitates to fill the gap of high temperature lightweight structural material.

Current methods are limited to using alloys with additions such as Ce, Zr, Mn, and Fe to achieve a moderate volume fraction of reinforcement.[8] In addition to thermal stability, the introduction of reinforcements increases stiffness of AM aluminum, minimizing undesirable deflection in structural applications, especially for those requiring high precision. Although bimetallic materials can also be used for stiffness modifications, their fabrication is largely limited to metallic intermetallic laminates, which lacks dimensional freedom comparing to powder-based AM.[9]

To address these challenges and limitations, we propose ''*In situ* Reactive Printing'' (IRP), a novel processing method based on current AM processes, to fabricate metal matrix composite that encompasses refined and dispersed *in situ* reaction product from using elemental powder mix as feedstock. Printability improvement as well as property enhancements root from an intermetallic phase formed via reactions in matrix material during printing. During IRP, elemental powders of dissimilar chemistry will react with each other under the influence of rapid heating and cooling that are unique to AM. In comparison with conventional manufacturing methods, the rapid solidification in AM could be beneficial to achieve refined reaction products,[10] while the Marangoni effect-driven high flow velocity in the melt pool[11] could result in the dispersion of secondary phases in the matrix material.

We added titanium powder to pure aluminum powder in IRP feedstock powder mix to modify the laser absorptivity of aluminum. This is aimed to promote better fusion of the powder and more stable melt pool. Adding titanium powder also enables reaction forming reinforcement intermetallic phase that enhances the material's mechanical properties such as stiffness. To achieve high volume fraction of intermetallic phases, elemental powder mix is used instead of prealloyed powder. Using elemental powder removes the alloying step and overcomes the low solubility problem of titanium in aluminum,[12] which means more intermetallic reinforcement phase can form in IRP.

Elimination of alloying step also avoids the presence of intermetallic phases in feedstock material, which can be challenging to process in AM due to their high melting temperature and brittle nature. While adding elements such as Fe, Ni, and Cu has been studied in the literature to improve AM of aluminum by *in situ* alloying, the focus of those studies is on alloying with aluminum and the formation of intermetallics is rather a by-product.[13–15] Alternatively, the enhancement of AM aluminum in the current work is achieved through creating a metallic–intermetallic composite material, aiming to possess characteristics that are superior to the parent aluminum matrix with the addition of titanium aluminide reinforcements.[16]

In this work, the concept of IRP and its effect on printability of aluminum in AM are discussed. The microstructure of samples printed with various mixing ratio of Ti/Al is studied. Direct correlation is found between feedstock powder mixing ratio and reinforcement volume fraction in as-printed samples. Tunability of mechanical performance of titanium aluminide-reinforced aluminum matrix composite (AMC) is shown using microhardness testing and nanoindentations. Results demonstrate that material in current work has a superior volume fraction of intermetallic reinforcement compared with other competing aluminum alloys or AMCs while pushing the envelope of stiffness improvement in AM-processed aluminum to a new level.

Materials and Methods

Sample preparation

Elemental powder mix of commercially pure (CP) titanium and CP aluminum was used as feedstock for IRP. CP titanium powders of particle size 45 to 106 μm from AP&C and CP aluminum powders of particle size 45 to 150 μm from Valimet were mixed in stainless steel vials for 30 min using SPEX8000 mixer/mill. The mixing vial was argon-filled to prevent oxidation of powders. Thirty minutes of mixing was performed in three 10 min intervals to reduce powder heating. Mixed powders showed good homogeneity, and no powder lumps were present (Supplementary Fig. S1d).

No ball milling media was used in the mixing process to avoid excessive aluminum powder deformation and formation of powder lumps that were observed in prior testing with use of milling media (Supplementary Fig. S1e). Powder was mixed with titanium content in weight percent of 10wt%, 20wt%, 30wt%, and 40wt% to systematically study the effect of powder composition on final print composition and microstructure. Powder clumps were discovered post-mixing on some occasions and were broken up thoroughly before being added into the powder feeder for printing.

IRP was performed on a FormAlloy X2 DED system equipped with an IPG Nd:YAG continuous wave fiber laser with 500 W max power at spot size of 1.2 mm. Build chamber was purged with argon to reduce oxygen level to below 100 ppm. Samples of $20 \times 8 \times 2$ mm were printed on CP-Ti substrates for each powder mix using rectilinear infill scan strategy with hatch spacing of 0.6 mm and angle offset of +67° and −67° in alternating layers with 0.2 mm layer height (Fig. 1a, b). The optimization criteria for print parameters were chosen to minimize pore and crack formation in printed samples.

At high energy densities, *in situ* reaction forms large patches of intermetallic, which is prone to cracking due to their brittle nature and presence of residual stresses. However, low energy density causes lack of fusion and therefore large number of pores in samples. The print quality was examined by optical imaging of polished section of each printed sample. Optimal print parameters were determined to be 300 W for laser power, 1500 mm/min for scanning speed, and volumetric feed rate of 0.93 cm^3/min (calculated using apparent density of elemental powders). All print parameters were held constant for printing the final samples used in this study. The samples are denoted by Ti10, Ti20, Ti30, and Ti40 corresponding to their titanium content in the powder mix.

Material characterization

For compositional and microstructural studies, all samples were sectioned into multiple pieces along the width (8 mm edge) using a high-speed diamond saw and polished to 0.02 μm with colloidal silica solution. Optical microscopic (OM) images of 50× magnification were taken for all samples

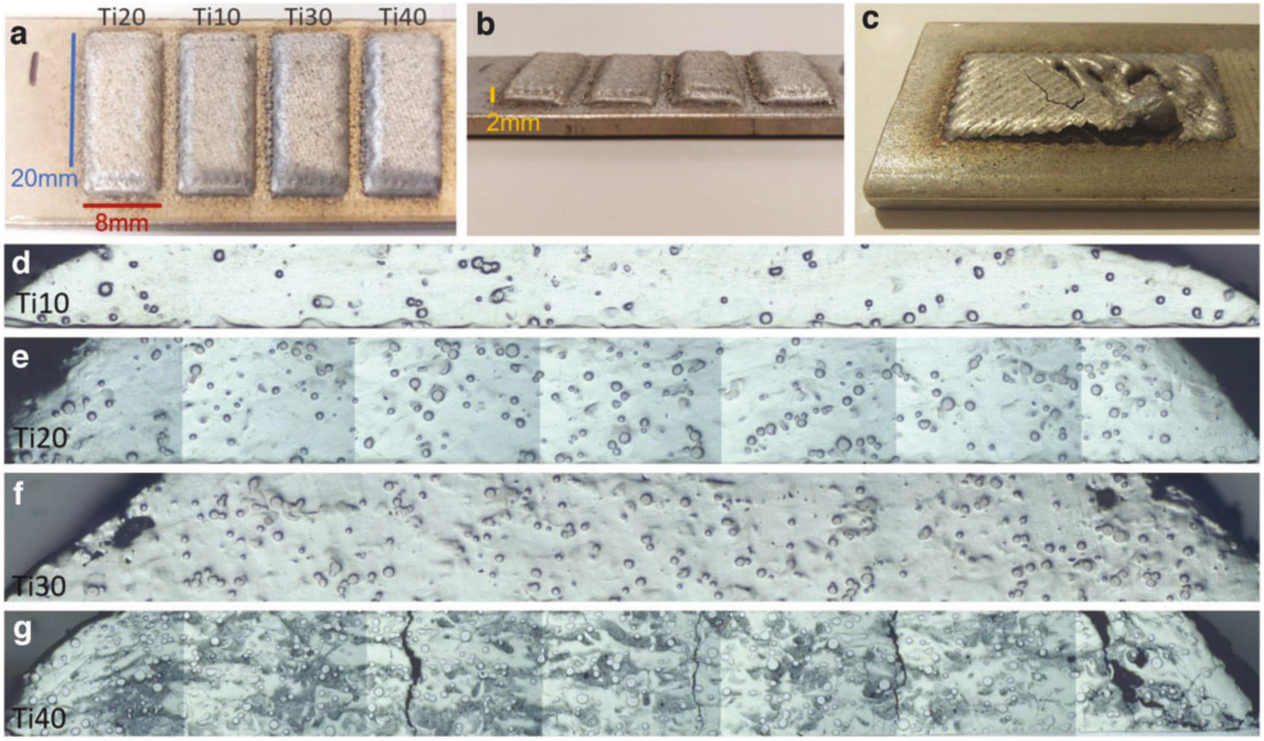

FIG. 1. Images of as-printed Ti/Al AMC samples' **(a)** top view, **(b)** side view, **(c)** image of attempted CP-Al print on CP-Ti substrate. Stitched optical microscope images of the cross section of **(d)** Ti10, **(e)** Ti20, **(f)** Ti30, and **(g)** Ti40 samples. AMC, aluminum matrix composite; CP, commercially pure. Color images available online.

to check for macroscopic cracks and pores. Scanning electron microscopy (SEM) scans using scanning electron and backscattered electron (BSE) detectors were performed on all samples with 25 keV beam voltage. All electron microscopy and further energy-dispersive X-ray spectroscopy (EDS) scans were performed in a Tescan Mira Field Emission SEM. BSE image of samples from each powder mix was analyzed with the ImageJ threshold function to determine the volume fraction of secondary phases in the aluminum matrix using their gray value histograms.

Lower and higher bounds of the threshold were held constant for the analysis. Electron backscatter diffraction (EBSD) analysis was performed on a Ti10 sample near the center of the cross section for phase identification and grain size measurements. The EBSD data were collected using an Oxford AZTEC EBSD system with a Nordlys EBSD camera at 15 kV and 0.25 μm step size over a scan area of $250 \times 190\,\mu$m. X-ray diffraction (XRD) analysis was performed on the polished surface of Ti30 samples with 2-theta values ranging between 10° and 90° to confirm the composition of the secondary phases in the aluminum matrix. Ti40 samples were excluded from the analysis due to the presence of detrimental cracks.

Samples used for SEM, BSE, EDS, and XRD characterizations were further tested for mechanical characteristics. One polished sample piece was randomly selected from the sectioned pieces of Ti10, Ti20, and Ti30 samples for microhardness testing using a Nanovea digital microhardness tester with a Vickers indenter tip. Indent force of 980.7 mN and hold time of 20 s were used for all indentations with a 0.4 mm spacing between adjacent indentations. Modulus of elasticity of each sample was calculated using the rule of mixtures, with modulus of elasticity of Al, Ti, and $TiAl_3$ taken as 69, 120, and 216 MPa, respectively.[17]

Experimental validation for modulus of elasticity was performed on a polished section of Ti10 sample using Alemnis nanoindenter equipped with a Berkovich indenter tip. Constant strain rate of $0.1\ s^{-1}$ was used for the loading and unloading of all nanoindentations with 400 mN peak load and no holding. Experimental elasticity was calculated from the average of the second-order polynomial fit and power law fit on the initial unloading curve in the range of 2% from peak displacement to 40% from zero displacement (Supplementary Fig. S2).

Results and Discussion

Improvement in printability of aluminum

Adoption of aluminum in AM has been hindered by properties including low absorptivity and a large solidification range.[18] These cause a detrimental effect in the form of unstable melt pool and solidification cracking. Multilayer prints of CP-Al were attempted in the current study to understand the difficulties in aluminum AM, and the result shows evidence of melt pool instability from material balling as well as visible solidification cracks (Fig. 1c). As printed Ti10, Ti20, and Ti30 samples, however, show a great improvement in printability, evident from their near-fully dense structure with no cracks and minimal to no porosities (Fig. 1d–f). This improvement is attributed to two major factors: better local thermal conditions during printing and the circumvention of solidification cracks.

The addition of Ti powder in the feedstock contributes to better thermal conditions via increased laser absorption compared with pure aluminum powder. This increase is supported by results from theoretical calculations, which shows that the titanium powder has an absorptivity almost eight times that of aluminum powder in DED conditions.[18] The calculations model powder particles in various conditions, including isolated spheres illuminated by a uniform laser beam, which resembles the DED process. Enhancing aluminum powder particles with both surface-coated and embedded nano-sized reinforcing materials can also reduce the reflectivity of aluminum, improving the printability of aluminum and resulting in better mechanical performance.[19]

However, powder enhancement is considerably more complicated and requires a special technique for powder feedstock fabrication, which renders IRP a cost-effective alternative for increasing the printability of aluminum powder. In addition, the negative enthalpy of mixing of titanium and aluminum,[20] accompanied by the negative formation enthalpy of Ti/Al intermetallic phases,[21] means additional energy is released into the melt pool. While the addition of titanium powder improves the thermal conditions during heating and melting of feedstock powder, the mixing and reactions unique to IRP improve the thermal conditions of the melt pool during cooling, which helps mitigate the solidification cracking problem often induced by localized high cooling rate in AM processes.

In addition to melt pool stabilization and reduction of solidification cracking problem, IRP also avoids reinforcement agglomeration, which is common in conventional AMC production. Reinforcement agglomeration is still a present challenge in creating a high volume fraction intermetallic-reinforced metal matrix materials using AM since agglomerates reduce the surface area of intermetallic powder and cause unfused volume or microcracks.[22] By using elemental powder mix as feedstock, IRP eliminates intermetallic agglomeration and thus enables the production of AMC material with a much higher reinforcement volume fraction. The increased intermetallic volume fraction threshold has a great potential in improving mechanical performance, which is discussed in detail in the Mechanical Performances section.

Moreover, a convective heat transfer phenomenon common to AM, Marangoni effect,[23] promotes the mixing of molten aluminum and titanium. This promoted mixing is in excellent agreement with the dispersed arrangement of intermetallic reinforcement (Fig. 2a), which is further discussed in the Dual-Phase Reinforcements and Tunable Intermetallic Volume Fraction section. However, a threshold still exists for the intermetallic volume fraction in AMC printed with IRP. When said threshold is surpassed, macrocracks form in a large volume of connected intermetallic reinforcement, as shown in Ti40 samples (Fig. 1e).

Dual-phase reinforcements and tunable intermetallic volume fraction

The cross sections of Ti10, Ti20, and Ti30 samples show a unified microstructure of aluminum matrix material with intermetallic reinforcements formed from *in situ* reactions and embedded unmelted titanium particles (Fig. 2a). Intermetallic reinforcements are formed primarily in needle shapes (middle arrow) while the remaining small portion consists of groups of near-equiaxed shapes arranged in a single profile (top arrow). No preferred orientation is present

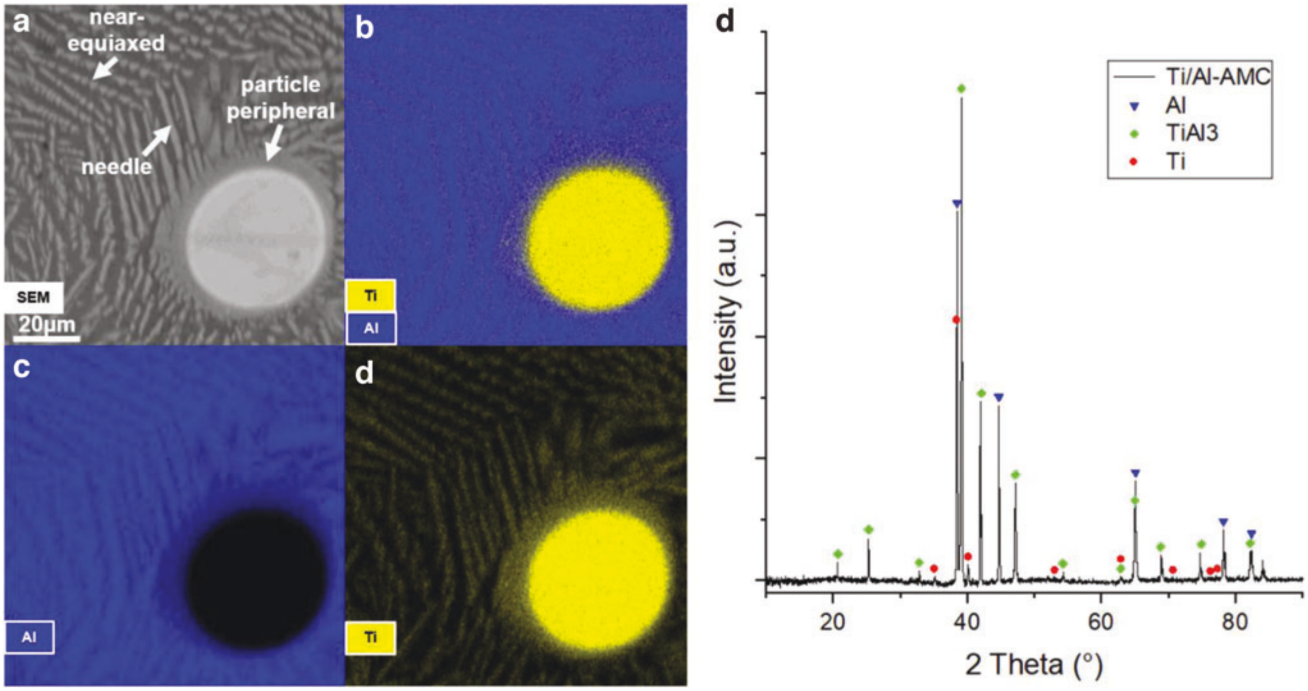

FIG. 2. EDS images of area around a retained titanium particle with dendritic reinforcing phases including **(a)** SEM (the *arrows* mark different intermetallic morphologies), **(b)** overlay of Ti and Al distribution, **(c)** Al distribution, and **(d)** Ti distribution. **(e)** XRD result of Ti30 sample with major peaks identified. EDS, energy-dispersive X-ray spectroscopy; SEM, scanning electron microscopy; XRD, X-ray diffraction. Color images available online.

for the acicular reinforcement phase. Intermetallic is also present at the interface of unmelted titanium particle and the matrix (bottom arrow).

EDS was performed on Ti30 samples to confirm that the secondary phase present in aluminum matrix is indeed intermetallic compound (IMC) of titanium and aluminum, as shown in the image of titanium and aluminum distributions overlayed (Fig. 2b). However, the Ti-Al binary phase diagram indicates that several types of IMCs can be formed between titanium and aluminum, including TiAl, $TiAl_2$, $TiAl_3$, Ti_2Al_5, and Ti_3Al.[24] To identify the type of IMC present in the system of the current study, XRD was performed on Ti30 samples, which contain the highest amount of IMC in the matrix (Fig. 2e). The peaks in the XRD result match well with $TiAl_3$ peaks. According to the Ti-Al binary phase diagram, $TiAl_3$ is the most probable reaction product when aluminum is abundant (more than 62wt%).[25]

In addition, $TiAl_3$ is the most favorable reaction product in the current system both from thermodynamics and from diffusion kinetics standpoints. At estimated DED melt pool temperature of 2000K, which is more than the melting temperature of titanium, the free energy of formation of $TiAl_3$ is −19,619 J/mol, much lower than that of Ti_3Al and TiAl, which are −16,218 and −3858 J/mol, respectively. It is important to note that $TiAl_2$ and Ti_2Al_5, the other possible titanium aluminides, can only form through reactions involving TiAl as one of the reagent, thus are omitted in comparison of free energy of formation.[24–26] The formation enthalpy of $TiAl_3$ is −2.96 kJ/mol, also much lower than that of Ti_3Al and TiAl, which are −0.67 and −1.52 kJ/mol, respectively.[27] These evidence indicate that the main reaction between titanium and aluminum is as follows:

$$\mathrm{Ti} + 3\mathrm{Al(L)} \overset{\text{yields}}{\rightarrow} \mathrm{TiAl_3}$$

The retained titanium particles are most likely a result of insufficient melting during processing and thus not included in the main reaction formula. Extensive experimental studies on diffusion couple/metallic intermetallic laminates as well as reactive sintering of titanium and aluminum also uphold the conclusion that $TiAl_3$ is the most favorable IMC formed between aluminum and titanium at high temperature (around and above the aluminum melting temperature) with an abundance of aluminum.[27–30]

As-printed Ti10, Ti20, and Ti30 samples were all nearfully dense without cracks but show visibly different amounts of acicular intermetallic reinforcement in the OM images. BSE images were taken to analyze the composition quantitatively using image analysis (samples of BSE images are shown in Fig. 3b–d). Thresholding of the BSE images to identify the different morphological phases was performed using the ImageJ over/underthreshold function. The brightest phase in the BSE images was identified as retained titanium particles, and the dark background was identified as aluminum matrix while the remaining of the image was identified as the intermetallic phase (Supplementary Fig. S3).

The volume fraction of retained titanium particle was taken directly from the gray value histogram, whereas the volume fraction of intermetallic is calculated with its gray value histogram percentage over the sum of the intermetallic phase and the matrix material. The results from the image analysis (Fig. 3a) show that Ti20 and Ti30 samples have high intermetallic volume fractions (55–60%) unattainable with other types of AMCs. The result also clearly indicates a correlation between the titanium content in the feedstock powder mix and the volume fraction of acicular intermetallic reinforcement as well as that of the retained titanium particles.

It is worth noting that comparing with the trend of volume fraction of retained titanium particles, volume fraction of intermetallic reinforcement shows much less increase in response to titanium addition when titanium content in feedstock is already high. This plateau phenomenon in the tunability of the intermetallic volume fraction hints the matrix reaching saturation. Small patches of intermetallic (marked by arrows) in BSE image of Ti30 samples (Fig. 3d) confirm the matrix being incapable of forming additional disperse acicular reinforcements.

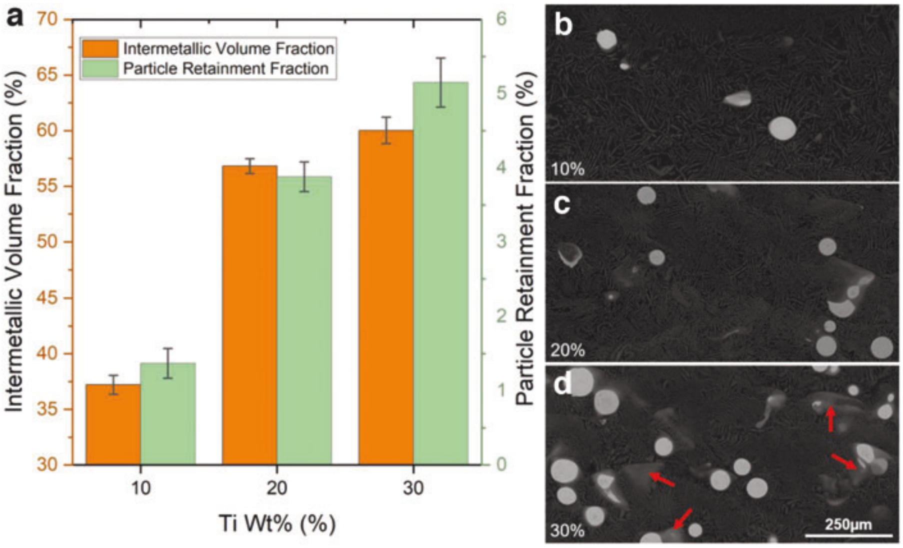

FIG. 3. **(a)** Intermetallic volume fraction versus Ti weight percentage from the image analysis. BSE images of microstructures for **(b)** Ti10, **(c)** Ti20, and **(d)** Ti30 (the *arrows* mark small patches of intermetallic) at the same magnification. BSE, backscattered electron. Color images available online.

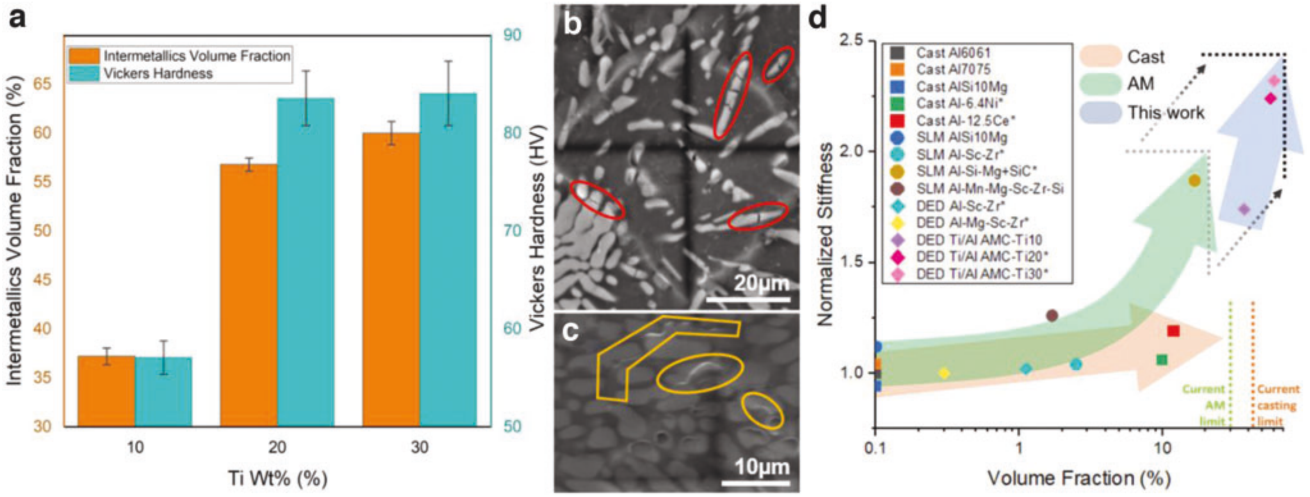

FIG. 4. **(a)** Hardness result; BSE images of indents on **(b)** Ti10 and **(c)** Ti30 with respective scale bars (*grey lines* marks post-indent features of interest detailed in section: Mechanical performances); and **(d)** Ashby plot of normalized stiffness (against pure Al) versus reinforcement volume fraction of different types of aluminum alloy/matrix composite. Readers are encouraged to explore the web version of this article for best visualization of these figures. *Elastic modulus calculated theoretically using the rule of mixture. Coolr images available online.

Mechanical performances

Hardness results show expected correlation with intermetallic volume fraction as well as plateau similar to that shown in the trend of intermetallic volume faction (Fig. 4a). All hardness values are taken from the average of 15 valid indents (indents that are not in the vicinity of unmelted particle) per sample. In addition, BSE images were taken post-indents. Fractures of acicular intermetallic phase (indicated by marking in red in Fig. 4b) and shifts of matrix material (indicated by marking in orange in Fig. 4c) were observed near some indents. In addition, to compare the stiffness of materials in the current study with those of the existing aluminum alloys and AMCs, the nanoindentation technique was used to determine the elasticity of Ti10 samples.

The peak load was chosen to create an indentation large enough to represent the composite material as a whole, thus avoiding false results from localized properties of matrix or reinforcement materials alone. The result of 119.8 ± 5.9 GPa elastic modulus was obtained from average of five indents on the tested Ti10 sample. The theoretical elasticity of Ti10 samples was also calculated using the rule of mixture, yielding 124.4 GPa with average intermetallic volume fraction measured before. Comparison between experimental measurement and theoretical calculation of Ti10 sample elasticity showed <4% error, confirming that the rule of mixture is applicable to AMC in the current study. Therefore, elasticity values for Ti20 and Ti30 samples were calculated using the rule of mixture due to loading limit of the nanoindentation setup.

The combined results of stiffness measurement and calculation are plotted in an Ashby plot (Fig. 4d) with other data points compiled from the relevant literature.[31–38] The Ashby plot shows that previous studies on aluminum AM have brought the volume fraction of reinforcement close to the level achieved by conventional manufacturing of AMCs while moderately increasing stiffness. Additionally on the same Ashby plot, the current state of the art in terms of high reinforcement volume fraction achieved in both AM (marked by green dotted line) and conventional methods

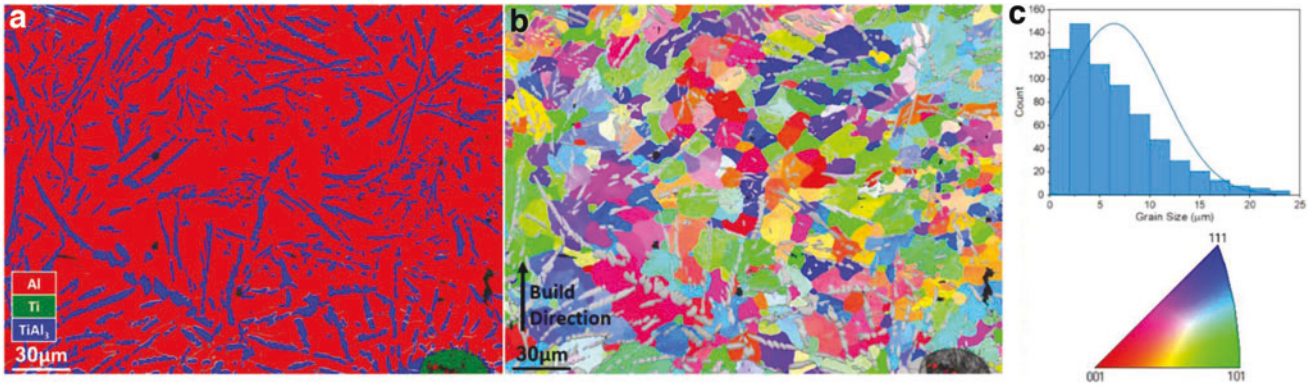

FIG. 5. **(a)** Phase map of EBSD analyzed region with Al, Ti, and $TiAl_3$ indexed in *grey*, respectively. **(b)** IPF-z from EBSD analysis with *black* and *grey* index shown on *bottom right*. **(c)** Size distribution of matrix aluminum grains. EBSD, electron backscatter diffraction; IPF, inverse pole figure. Color images available online.

(marked by orange dotted line) is presented as reference values for comparison.[39,40]

AMCs fabricated with IRP shows even further improvement in volume fraction of intermetallic reinforcement up to 60% as well as in stiffness when compared with existing alloys and AMCs. In addition, comparing with cast AMCs, higher cooling rate in AM results in the finer scale intermetallic in AMCs fabricated with IRP. This intermetallic refinement could be more beneficial for mechanical property enhancement, complimentary to volume fraction increase from 42% in cast AMCs to 60% in AMCs fabricated with IRP. Refined grain size is also observed in the matrix aluminum as shown in the inverse pole figure from EBSD analysis (Fig. 5b) with distribution of intermetallic phase shown in the phase map (Fig. 5a).

Six hundred eighty-six grains in the matrix aluminum were detected in the EBSD analysis, with the average grain size of $14.75 \pm 4.38\,\mu$m for the 100 largest grains (Fig. 5c), which is a good representation of grain size to help eliminate noise from smaller features/indexing errors. This shows great grain refinement in AMCs produced with IRP in comparison to average grain size of 200–500 μm in as-cast wrought aluminum alloys or average grain size of 100–150 μm in cast ingots of commercial purity aluminum.[41,42] This refinement in aluminum grain size is likely due to combined effect of fast solidification as well as formation of $TiAl_3$, which can promote nucleation events and reduce grain growth. This is also supported by the data available in the literature, suggesting that $TiAl_3$ can act as heterogeneous nucleation sites in grain refinement of CP aluminum.[43]

While the ultra-high volume fraction of intermetallic reinforcement undoubtedly contributes to the stiffness enhancement, it also lends itself to improving the thermal stability of the printed AMC given the high melting temperature of $TiAl_3$. Furthermore, the low solubility of titanium in the aluminum matrix material is expected to inhibit reinforcement coarsening at an elevated temperature. In addition, the matrix aluminum shift indicated by the ripple around the indentation (marked region in Fig. 4c) also shows some retained ductility from aluminum being the matrix material. In addition, the tunability of mechanical characteristics from different mixing ratio of the feedstock also allows *in situ* compositional adjustment using powder-based DED AM, giving the designer much more freedom to create components with site-specific properties.

Conclusions

This study presents IRP as a novel method to fabricate tunable titanium aluminide ($TiAl_3$)-reinforced AMC capable of reaching intermetallic volume fraction up to 60%. The successful production of AMC with enhanced properties demonstrates that IRP can harness the rapid cyclic thermal conditions of AM to form reinforcing reaction product *in situ*. The obtained AMC material with large amount of refined and well-dispersed secondary phases also shows evident improvement in AM processability of aluminum. Different feedstock compositions were tested to systematically study the effect of powder composition on final print composition and microstructure. Feedstock containing 10wt%, 20wt%, and 30wt% titanium showed printability improvement and compositional tunability.

Feedstock containing 40wt% titanium showed detrimental through-height cracks, revealing maximum intermetallic capacity of aluminum matrix. Mechanisms contributing to printability improvement and microstructure features of AMC fabricated with IRP are feedstock laser absorption enhancement, exothermic mixing of elemental material leading to the formation of intermetallic reinforcements. Finally, IRP is experimentally shown in the current study to achieve a much higher volume fraction of intermetallic and consequently higher stiffness than that of other aluminum alloys or AMCs. These promising results encourage future investigations on macroscale mechanical performances such as tensile, fatigue, and wear properties as well as thermal stability of this alloy system. While the current study focuses on the Ti/Al material couple, we believe that IRP is applicable to other material systems to create metal matrix composites with enhanced mechanical performance from high volume fraction of intermetallic reinforcement.

Acknowledgments

The authors would like to acknowledge Hassani Group at Cornell University for performing nanoindentation experiments with subsequent data analysis and Ronald Davis at Corning Glass for performing EBSD data collection with subsequent data processing.

Authors' Contributions

C.T.: Conceptualization (equal), methodology (equal), investigation (lead), data curation (lead), visualization (lead), formal analysis (lead), writing—original draft (lead), and writing—review and editing (equal). A.M.: Conceptualization (equal), methodology (equal), supervision (lead), validation (lead), and writing—review and editing (equal). All persons who meet the authorship criteria are listed as authors, and all authors certify that they have participated sufficiently in the work to take public responsibility for the content, including participation in the concept, design, analysis, writing, or revision of the article.

Author Disclosure Statement

No competing financial interests exist.

Funding Information

Atieh Moridi acknowledges financial support from the National Science Foundation CAREER Award (CMMI-2046523) and the Office of Naval Research Young Investigator Award (N00014-22-1-2420). This work made use of the Cornell Center for Materials Research Shared Facilities, which are supported through the NSF MRSEC program (DMR-1719875).

Supplementary Material

Supplementary Figure S1
Supplementary Figure S2
Supplementary Figure S3

References

1. Haghdadi N, Laleh M, Moyle M, et al. Additive manufacturing of steels: A review of achievements and

challenges. J Mater Sci 2021;56(1):64–107; doi: 10.1007/s10853-020-05109-0

2. Tian Z, Zhang C, Wang D, et al. A review on laser powder bed fusion of inconel 625 nickel-based alloy. Appl Sci 2020;10(1):10081; doi: 10.3390/app10010081
3. Hosseini E, Popovich VA. A review of mechanical properties of additively manufactured inconel 718. Addit Manuf 2019;30:18; doi: 10.1016/j.addma.2019.100877
4. Liu Z, He B, Lyu T, et al. A review on additive manufacturing of titanium alloys for aerospace applications: Directed energy deposition and beyond Ti-6Al-4V. JOM 2021;73(6):1804–1818; doi: 10.1007/s11837-021-04670-6
5. Grover T, Pandey A, Kumari ST, et al. Role of titanium in bio implants and additive manufacturing: An overview. Mater Today 2019;2019:3071–3080; doi: 10.1016/j.matpr.2020.02.636
6. Mertens AI, Delahaye J, Lecomte-Beckers J. Fusion-based additive manufacturing for processing aluminum alloys: State-of-the-art and challenges. Adv Eng Mater 2017;19(8):170003; doi: 10.1002/adem.201700003
7. Trapp J, Rubenchik AM, Guss G, et al. In situ absorptivity measurements of metallic powders during laser powder-bed fusion additive manufacturing. Appl Mater Today 2017;9:341–349; doi: 10.1016/j.apmt.2017.08.006
8. Michi RA, Plotkowski A, Shyam A, et al. Towards high-temperature applications of aluminium alloys enabled by additive manufacturing. Int Mater Rev 2021;67(3):298–345; doi: 10.1080/09506608.2021.1951580
9. Amirkhanlou S, Ji S. A review on high stiffness aluminum-based composites and bimetallics. Crit Rev Solid State Mater Sci 2020;45(1):1–21; doi: 10.1080/10408436.2018.1485550
10. Ji X, Mirkoohi E, Ning J, et al. Analytical modeling of post-printing grain size in metal additive manufacturing. Opt Lasers Eng 2020;124:105805; doi: 10.1016/j.optlaseng.2019.105805
11. Guo Q, Zhao C, Qu M, et al. In-situ full-field mapping of melt flow dynamics in laser metal additive manufacturing. Addit Manuf 2020;31:100939; doi: 10.1016/j.addma.2019.100939
12. Dezellus O, Gardiola B, Andrieux J, et al. On the solubility of group IV elements (Ti, Zr, Hf) in liquid aluminum below 800°C. J Phase Equilibria Diffus 2014;35(2):120; doi: 10.1007/s11669-013-0278-2ï
13. Qi X, Takata N, Suzuki A, et al. Laser powder bed fusion of a near-eutectic Al–Fe binary alloy: Processing and microstructure. Addit Manuf 2020;35:101308; doi: 10.1016/j.addma.2020.101308
14. Jandaghi MR, Aversa A, Manfredi D, et al. In situ alloying of AlSi10Mg-5 wt% Ni through laser powder bed fusion and subsequent heat treatment. J Alloys Compd 2022;904:164081; doi: 10.1016/j.jallcom.2022.164081
15. Martinez R, Todd I, Mumtaz K. In situ alloying of elemental Al-Cu12 feedstock using selective laser melting. Virtual Phys Prototyp 2019;14(3):242–252; doi: 10.1080/17452759.2019.1584402
16. Chak V, Chattopadhyay H, Dora TL. A review on fabrication methods, reinforcements and mechanical properties of aluminum matrix composites. J Manuf Process 2020;56:1059–1074; doi: 10.1016/j.jmapro.2020.05.042
17. Song YL, Dou ZH, Zhang TA, et al. First-principles calculation on the structural, elastic and thermodynamic properties of Ti-Al intermetallics. Mater Res Express 2019;6(10):ab3e11; doi: 10.1088/2053-1591/ab3e11
18. Boley CD, Khairallah SA, Rubenchik AM. Calculation of laser absorption by metal powders in additive manufacturing. Addit Manuf Handb 2017;2017:507–517; doi: 10.1201/9781315119106
19. Lin TC, Cao C, Sokoluk M, et al. Aluminum with dispersed nanoparticles by laser additive manufacturing. Nat Commun 2019;10(1):4124; doi: 10.1038/s41467-019-12047-2
20. Men H, Fan Z. An analytical model for solute segregation at liquid metal/solid substrate interface. Metall Mater Trans A Phys Metall Mater Sci 2014;45(12):5508–5516; doi: 10.1007/s11661-014-2525-5
21. Delsante S, Ghosh G, Borzone G. A calorimetric study of alloys along the Ti(Zn, Al)3 section. CALPHAD 2009;33(1):50–54; doi: 10.1016/j.calphad.2008.08.003
22. Yeap SP. Permanent agglomerates in powdered nanoparticles: Formation and future prospects. Powder Technol 2018;323:51–59; doi: 10.1016/j.powtec.2017.09.042
23. Dass A, Moridi A. State of the art in directed energy deposition: From additive manufacturing to materials design. Coatings 2019;9(7):418; doi: 10.3390/COATINGS9070418
24. Kattner UR, Lin J-C, Chang YA. Thermodynamic assessment and calculation of the Ti-AI system. Metall Trans A 1992;23:2081–2090.
25. Su Jat A M, Bhargava S, Sangal S. On the formation of TiAl 3 during reaction between solid Ti and liquid Al. J Mater Sci Lett 1997;16(14):1175–1178.
26. Zhao Y, Li J, Qiu R, et al. Growth characterization of intermetallic compound at the Ti/Al solid state interface. Materials 2019;12(3):1–11; doi: 10.3390/ma12030472
27. Xu L, Cui YY, Hao YL, et al. Growth of intermetallic layer in multi-laminated Ti/Al diffusion couples. Mater Sci Eng A 2006;435–436:638–647; doi: 10.1016/j.msea.2006.07.077
28. Peng LM, Wang JH, Li H, et al. Synthesis and microstructural characterization of Ti-Al3Ti metal-intermetallic laminate (MIL) composites. Scr Mater 2005;52(3):243–248; doi: 10.1016/j.scriptamat.2004.09.010
29. Mirjalili M, Soltanieh M, Matsuura K, et al. On the kinetics of TiAl 3 intermetallic layer formation in the titanium and aluminum diffusion couple. Intermetallics (Barking) 2013;32:297–302; doi: 10.1016/j.intermet.2012.08.017
30. Školáková A, Leitner J, Salvetr P, et al. Kinetic and thermodynamic description of intermediary phases formation in Ti-Al system during reactive sintering. Mater Chem Phys 2019;230:122–130; doi: 10.1016/j.matchemphys.2019.03.062
31. Shakil SI, Hadadzadeh A, Shalchi Amirkhiz B, et al. Additive manufactured versus cast AlSi10Mg alloy: Microstructure and micromechanics. Results Mater 2021;10:100178; doi: 10.1016/j.rinma.2021.100178
32. Kürnsteiner P, Bajaj P, Gupta A, et al. Control of thermally stable core-shell nano-precipitates in additively manufactured Al-Sc-Zr alloys. Addit Manuf 2020;32:100910; doi: 10.1016/j.addma.2019.100910
33. Jia Q, Zhang F, Rometsch P, et al. Precipitation kinetics, microstructure evolution and mechanical behavior of a developed Al–Mn–Sc alloy fabricated by selective laser melting. Acta Mater 2020;193:239–251; doi: 10.1016/j.actamat.2020.04.015
34. Glerum JA, Kenel C, Sun T, et al. Synthesis of precipitation-strengthened Al-Sc, Al-Zr and Al-Sc-Zr alloys via selective laser melting of elemental powder blends. Addit Manuf 2020;36:101461; doi: 10.1016/j.addma.2020.101461
35. Chang F, Gu D, Dai D, et al. Selective laser melting of in-situ Al4SiC4 + SiC hybrid reinforced Al matrix compos-

ites: Influence of starting SiC particle size. Surf Coat Technol 2015;272:15–24; doi: 10.1016/j.surfcoat.2015.04.029

36. Aboulkhair NT, Maskery I, Tuck C, et al. The microstructure and mechanical properties of selectively laser melted AlSi10Mg: The effect of a conventional T6-like heat treatment. Mater Sci Eng A 2016;667:139–146; doi: 10.1016/j.msea.2016.04.092
37. Liu Y, Michi RA, Dunand DC. Cast near-eutectic Al-12.5 wt.% Ce alloy with high coarsening and creep resistance. Mater Sci Eng A 2019;767:138440; doi: 10.1016/j.msea.2019.138440
38. Fuller CB, Seidman DN, Dunand DC. Mechanical properties of Al(Sc,Zr) alloys at ambient and elevated temperatures. Acta Mater 2003;51(16):4803–4814; doi: 10.1016/S1359-6454(03)00320-3
39. Plotkowski A, Sisco K, Bahl S, et al. Microstructure and properties of a high temperature Al–Ce–Mn alloy produced by additive manufacturing. Acta Mater 2020;196:595–608; doi: 10.1016/j.actamat.2020.07.014
40. Fodran EJ. Microstructural Evolution and Thermal Stability of Al-Ce-Ni Ternary Eutectic. Florida; 2002. Available from: https://www.proquest.com/pagepdf/276240246?accountid=10267 [Last accessed: June 29, 2022].
41. Easton M, Davidson C, St. John D. Grain morphology of As-Cast wrought aluminium alloys. Mater Trans 2011;52(5): 842–847;; doi: 10.2320/matertrans.L-MZ201118
42. Kashyap KT, Chandrashekar T. Effects and mechanisms of grain refinement in aluminium alloys. Bull Mater Sci 2001; 24(4):345–353.
43. Chen Z, Yan K. Grain refinement of commercially pure aluminum with addition of Ti and Zr elements based on crystallography orientation. Sci Rep 2020;10(1):16591; doi: 10.1038/s41598-020-73799-2

Address correspondence to:
Atieh Moridi
Sibley School of Mechanical and Aerospace Engineering
Cornell University
124 Hoy Road
Upson Hall
Ithaca, NY 14850
USA

E-mail: moridi@cornell.edu